CHEMISTRY OF MATERIALS

Article

pubs.acs.org/cm

Structural Evolution of Reversible Mg Insertion into a Bilayer Structure of $V_2O_5{\cdot}nH_2O$ Xerogel Material

Niya Sa,*[,†,‡] Tiffany L. Kinnibrugh,[#] Hao Wang,[†,‡] Gopalakrishnan Sai Gautam,[§] Karena W. Chapman,[#] John T. Vaughey,[†,‡] Baris Key,[†,‡] Timothy T. Fister,[†] John W. Freeland,[#] Danielle L. Proffit,[†,‡] Peter J. Chupas,[#] Gerbrand Ceder,[§] Javier G. Bareno,[‡] Ira D. Bloom,[‡] and Anthony K. Burrell*[,†,‡]

[†]Joint Center for Energy Storage Research, [‡]Chemical Science and Engineering Division, and [#]X-ray Science Division, Advanced Photon Source, Argonne National Laboratory, Lemont, Illinois 60439, United States

[§]Material Science Division, Lawrence Berkeley National Laboratory, Berkeley, California 94720, United States

Supporting Information

ABSTRACT: Functional multivalent intercalation cathodes represent one of the largest hurdles in the development of Mg batteries. While there are many reports of Mg cathodes, many times the evidence of intercalation chemistry is only circumstantial. In this work, direct evidence of Mg intercalation into a bilayer structure of $V_2O_5{\cdot}nH_2O$ xerogel is confirmed, and the nature of the Mg intercalated species is reported. The interlayer spacing of $V_2O_5{\cdot}nH_2O$ contracts upon Mg intercalation and expands for Mg deintercalation due to the strong electrostatic interaction between the divalent cation and the cathode. A combination of NMR, pair distribution function (PDF) analysis, and X-ray absorption near edge spectroscopy (XANES) confirmed reversible Mg insertion into the $V_2O_5{\cdot}nH_2O$ material, and structural evolution of Mg intercalation leads to the formation of multiple new phases. Structures of $V_2O_5{\cdot}nH_2O$ with Mg intercalation were further supported by the first principle simulations. A solvent cointercalated Mg in $V_2O_5{\cdot}nH_2O$ is observed for the first time, and the ^{25}Mg magic angle spinning nuclear magnetic resonance (MAS NMR) spectroscopy was used to elucidate the structure obtained upon electrochemical cycling. Specifically, existence of a well-defined Mg−O environment is revealed for the Mg intercalated structures. Information reported here reveals the fundamental Mg ion intercalation mechanism in a bilayer structure of $V_2O_5{\cdot}nH_2O$ material and provides insightful design metrics for future Mg cathodes.

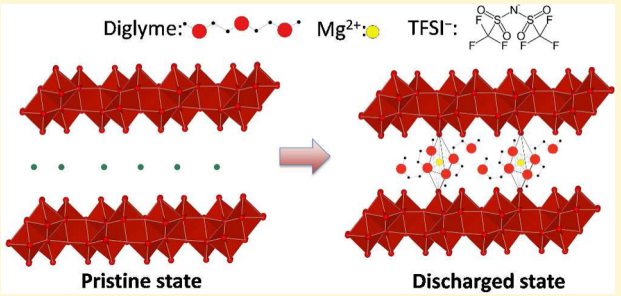

INTRODUCTION

Lithium ion batteries (LIBs) are ubiquitously applied as energy storage devices, but with increasing demands for our automotive needs, batteries with a greater energy density are a necessity.[1] The possibility that Mg batteries can exceed the energy density of Li-ion cells has drawn significant interest from the battery community in recent years and is a major driving force behind efforts to create a rechargeable Mg battery.[2] Magnesium may enable the use of a metallic anode and has many positive attributes such as abundance, high theoretical volumetric capacity, and nondendritic growth when electrodeposited on a metal anode.[3,4] However, many challenges need to be addressed before realizing the full potential of Mg batteries. In particular, cathode materials for a Mg battery are typically limited to low voltage Chevrel-type materials (1.1 V vs Mg/Mg^{2+}). Electrolytes used with the Chevrel cathodes are Grignard-type reagents,[5−8] including magnesium organohaloaluminate[9−11] and organomagnesium halides systems.[11,6,12] To achieve high energy density, cathodes beyond Chevrel are a necessity. In particular, oxide electrodes are attractive, mainly due to their higher voltages and density that leads to high volumetric energy density. Unfortunately very few oxide cathodes for Mg have been reported, and most have low capacity or have been shown to undergo conversion reactions.[8,13−16] One issue that dominates the literature is the lack of understanding as to the nature of the Mg intercalation reactions within oxide hosts. Questions such as the local structure change of the materials upon Mg insertion/deinsertion, possible Mg insertion sites, and the corresponding structure evolution to the cathode material remain to be answered. A recent report has highlighted the compatibility of a halide free, low-water content Mg $(TFSI)_2$/diglyme-based electrolyte that is stable in contact with typical metal oxide cathodes.[17] While not optimal for efficient cycling, this system allows intercalation chemistry at a putative cathode in the absence of reactive halides and thus permits us to assess the intercalation and deintercalation pathways of Mg cations in oxide cathode materials.

Work presented here describes structural evolution of a bilayer structure of $V_2O_5{\cdot}nH_2O$ xerogel material with a wide

Received: January 4, 2016
Revised: March 31, 2016
Published: March 31, 2016

DOI: 10.1021/acs.chemmater.6b00026
Chem. Mater. 2016, 28, 2962−2969

interlayer spacing, for reversible Mg intercalation. $V_2O_5{\cdot}nH_2O$ (n = ~0.6) is composed of ribbon-like structural units that display lamellar ordering, with water molecules between the layers which are possibly bonded to an open coordination site on the vanadium cations.[18,19] Such a layered framework host is of great interest in Mg intercalation mostly owing to its structure flexibility and ability to adapt to the geometry of the intercalated guest species by adjusting the interlayer separation. Due to its rich intercalation chemistry and ability to insert a variety of cations, such as Na^+,[20] Mg^{2+},[21,22] Li^+,[23] this material has been studied by several groups seeking a well-established high voltage cathode owing to its single step reduction process centered around 3 V.[24,25] However, the structure of $V_2O_5{\cdot}nH_2O$ has remained elusive until recent years due to its weakly crystalline nature that hampered characterization.[25] Previously reported $V_2O_5{\cdot}nH_2O$ studies focused mainly on simple electrochemistry without describing the evidence for Mg intercalation.[21,22]

Herein, we combine an in-depth understanding of the structural evolution for $V_2O_5{\cdot}nH_2O$ upon Mg intercalation with the electrochemistry in a metal oxide stable Mg-based electrolyte. Results presented here confirm the proposed double layered $V_2O_5{\cdot}nH_2O$ with two sheets of V_2O_5 facing each other, referred to as a bilayer structure $V_2O_5{\cdot}nH_2O$ in the following context. Interestingly, the water molecules in the xerogel $V_2O_5{\cdot}nH_2O$ electrode are held in place in the cathode material during reversible Mg insertion and do not impact the use of Mg metal as an anode. High energy X-ray diffraction, coupled with pair distribution function analysis, showed a complex multiphase evolution of $Mg_xV_2O_5{\cdot}nH_2O$ with several different interlayer spacings. Results indicate that the average interlayer spacing of $V_2O_5{\cdot}nH_2O$ contracts upon Mg insertion and expands for Mg deinsertion. MAS NMR was used to understand the Mg environment of the discharged $Mg_x[V_2O_5{\cdot}nH_2O]$ product, and the results suggest two Mg environments with well-ordered oxygen coordination.

EXPERIMENTAL SECTION

Synthesis of $V_2O_5{\cdot}nH_2O$ Cathode. A 0.5 M solution of sodium metavanadate in water (Fluka, > 98%) was eluted through a proton exchange resin (Dowex 50 WX2, 50−100 mesh) filled column. A pale yellow effluent was collected afterward, followed with 3 days aging to obtain a homogeneous vanadium oxide hydrogel. To completely remove the physically absorbed water, collected hydrogel V_2O_5 was dried in a vacuum oven at 60 °C for 5 h, followed with another drying step where the container was attached to a vacuum pump for 12 h. The resulting dark red powder of V_2O_5 xerogel was applied to cast 8:1:1 weight-ratio slurry of V_2O_5 xerogel (Fluka, > 99%), Timcal Super C45 carbon black, and polyvinylidene fluoride (PVDF) dissolved in *N*-methyl-2-pyrrolidinone (NMP) onto a 304 stainless steel current collector. The as-prepared laminates were then dried at 75 °C in an oven for 1 h before being punched as 7/16″ diameter electrodes.

Synthesis of the $Mg(TFSI)_2$ Electrolyte. Magnesium bis(trifluoromethane sulfonyl)imide (99.5%, Solvionic, France) was dried in a vacuum oven located inside of an argon inert atmosphere at 180 °C for 24 h before use. Diglyme (Aldrich, anhydrous, 99.5%) solvent was pretreated with molecular sieves (Aldrich, 3 Å beads, 4−8 mesh) before dissolving magnesium bis(trifluoromethane sulfonyl)-imide. The as-prepared electrolyte was then stirred overnight before use.

Coin Cell Assembling and Electrochemical Characterization. Coin cells were assembled in an argon-filled glovebox using xerogel V_2O_5 as the cathode and a mechanically polished Mg disk (99.9% purity, Sigma-Aldrich) as the anode. $Mg(TFSI)_2$ in diglyme was used as an electrolyte with ~0.07 mL added in each coin cell. A glass fiber separator (Whatman, GF/F) was used between the electrodes. Galvanostatic cycling of the coin cells was performed using a Maccor series 4000 cycler at a current density of 20 $\mu A/cm^2$, with a voltage range of 0 to 3.2 V. Three electrode Swagelok cells were used for the cyclic voltammetry measurements, with xerogel V_2O_5 as the cathode and a polished Mg disk (7/16" diameter) as the counter and reference electrodes, respectively. Cyclic voltammetry was measured using a multichannel potentiostat (Parstat MC, Princetion Applied Research, TN) under a pure argon atmosphere in a glovebox, where H_2O and O_2 levels are kept under 1 ppm. 1.0 M $Mg(TFSI)_2$ in diglyme was applied as the electrolyte for both coin cells and swagelok cells. Cathode materials for X-ray absorption, X-ray scattering, and solid state NMR experiments were harvested inside of the glovebox after coin cells went through 10 cycles, before holding at a certain potential at either a charged or discharged state for about 20 h.

X-ray Absorption. Ex situ vanadium(V) K-edge X-ray absorption spectroscopy (XAS) was performed for charged and discharged cathodes at the beamline 20-BM-B at Advanced Photon Source (APS), Argonne National Lab (ANL). K-edge XAS were carried out in transmission mode with a vanadium metal foil as a reference. The XANES spectra were normalized and analyzed using the ATHENA software package. The edge position, located at the maximum of the first derivative, was defined as 5465 eV. The total resolution (including intrinsic broadening from the V 1s core-hole lifetime, incident slits, and the resolution of the silicon 111 monochromator) is ~0.6 at 5470 eV. Ex situ vanadium(V) L-edge spectra were acquired at beamline 4-ID-C at APS, ANL by simultaneous measurement of the surface sensitive electron yield (EY) and the bulk sensitive fluorescence yield (FY). The beamline resolution for L-edge spectra measurements was 0.1 eV. An oxygen reference standard was recorded at the same time for accurate energy alignment. Cycled coin cells were dissembled inside of an argon-filled glovebox. Cathode material was collected and vacuum-dried at room temperature for about 1 h before mixed homogeneously with cellulose at a mass ratio of 1:5 (inside of a glovebox). The mixture was then pressed into pellets and sealed inside of kapton tape. Samples were then transferred into the beamline for the XAS measurement using an argon filled glovebag.

X-ray Scattering and PDF Analysis. Electrode samples were recovered from different charged or discharged states from electrochemically cycled coin cells, and powder was collected and loaded in polyimide capillaries. X-ray total scattering data, suitable for PDF analysis, were collected at beamline 11-ID-B at the APS, ANL. High-energy X-rays (λ = 0.2114 Å) were combined with a large area detector (PerkinElmer amorphous-silicon) to collect data to high values of momentum transfer.[26,27] The scattering images were reduced to one-dimensional X-ray powder diffraction data within the FIT2D software.[28] The data were corrected for background scattering, compton scattering, and detector effects. Data was Fourier transformed to Q_{max} = 23 $Å^{-1}$ to obtain the PDF G(r) within PDFgetX2.[29] Structural models were refined against the PDF data within PDFgui.[30] The position and intensity of peaks of interest were quantified by fitting Gaussian functions to these features within FITYK.[31]

NMR Characterization. ^{25}Mg NMR spectra were collected for solid state synthesized MgV_2O_5 and electrochemically cycled $Mg_xV_2O_5$ at the spinning speed of 16 kHz at 190 °C. A magnetic field strength of 19.89 T was used in these experiments with a Varian Inova spectrometer, corresponding to a ^{25}Mg Larmor frequency of 52.22 MHz. The ^{25}Mg NMR spectra were acquired with rotor synchronized spin−echo experiments (90°-τ-180°-τ) where $\tau = n/\nu_r$ (ν_r: spinning speed in Hz) and a $\pi/2$ of 2 μs was used. The signals were referenced to a 5 M $MgCl_2$ aqueous solution at 0 ppm. Samples were packed into a 4 mm rotor under inert atmosphere and a total of 692347 scans (24 mg active weight in rotor, for electrochemical sample) and 23504 scans (100 mg active weight in rotor, for model compound) with a recycle delay of 1 s. ^1H, ^2H, and ^{13}C NMR spectra were collected on a Bruker Avance III spectrometer using a 1.3 mm probe operating at a spinning speed of 40 kHz (2.6, 0.5, 0, −0.2 V, pristine, and soaked/dried sample) at 100 °C, and a magnetic field strength of 7.02 T was used. Samples were packed into a 1.3 mm rotor post vacuum-dry in inert atmosphere for 3 h (Argon glovebox operating with <1.0 ppm

DOI: 10.1021/acs.chemmater.6b00026
Chem. Mater. 2016, 28, 2962−2969

water) for signal acquisition with near identical weights. ^{1}H NMR spectra are normalized to the weight of the active materials in rotors. ^{1}H and ^{13}C NMR signals were referenced to TMS at 0 ppm. The ^{2}H NMR signal was referenced to D_2O at 4.8 ppm at room temperature. Cross-polarization experimental conditions were optimized at a spinning speed of 10 kHz using adamantane.

First-Principles Calculations. The VASP code is applied to perform the first-principles calculations[32,33] with the vdW-DF2 exchange-correlation framework[34,35] that includes van der Waals interactions for calculating the layer spacing. A Hubbard U correction of 3.1 eV is added to remove the self-interaction errors in the d-electrons of vanadium.[35] Also, calculations are performed with a dense k-point grid and a plane wave cutoff of 520 eV. The intercalated Ni positions in the bilayered V_2O_5 structure, reported by Oka et al.,[36] are used as the initial Mg positions in the structure relaxation calculations.

RESULTS AND DISCUSSION

Reversible Mg Intercalation into $V_2O_5{\cdot}nH_2O$. Galvanostatic cycling tests were carried out on coin cells composed of a $V_2O_5{\cdot}nH_2O$ as the cathode, with a Mg metal disk as the anode at a current density of 20 μA/cm^2. The first 10 cycles of the charge−discharge curve are presented in Figure 1a, where

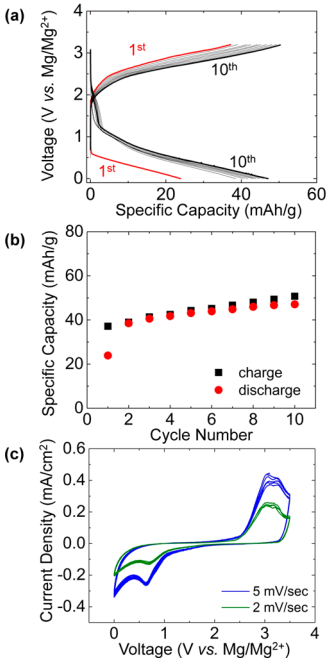

Figure 1. Electrochemical characterization of coin cells with $V_2O_5{\cdot}nH_2O$ as cathodes and Mg as anodes in 1.0 M $Mg(TFSI)_2$ diglyme electrolyte. (a) First 10 cycles of galvanostatic charge−discharge curves at current density of 20 μA/cm^2. (b) A typical capacity versus cycle number plot, where black squares represent charge capacity and red dots are discharge capacity. (c) Cyclic voltammetry at a scan rate of 2 mV/s (green) and 5 mV/s (blue). Five continuous cycles were shown for each case.

reversible insertion and deinsertion of Mg ions is observed. The overall cell voltage varied continuously without the appearance of apparent voltage plateaus, indicative of a typical insertion/deinsertion reaction of Mg^{2+} into the longer range disordered $V_2O_5{\cdot}nH_2O$ structure. To quantify the Mg content upon intercalation, integration of the current gave a discharge capacity of ∼50 mAh/g (or 0.25 mol Mg insertion per mole of the vanadium oxide).

A typical capacity versus cycle number plot is presented in Figure 1b, where no significant capacity decay was observed after 10 cycles, but a slightly gradual capacity escalation can be seen at cycle 10 as compared with the first cycle. Gains in capacity are ascribed to an increase of the microscopic reaction area accompanied by electrolyte penetration into the cathode material. Figure 1c shows typical cyclic voltammograms (CV) of $V_2O_5{\cdot}nH_2O$ versus Mg anode at a scan rate of 2 mV/s (green) and 5 mV/s (blue), with 5 continuous cycles, respectively. As the scan rate increases from 2 to 5 mV/s, the reduction peak shifted slightly to a more negative potential, while the oxidation peaks partly moved to a more positive potential value, suggesting the electrochemical insertion of Mg is a slow kinetic process. The CV results illustrate the presence of two unresolved anodic oxidation peaks around 3.0 V corresponding to the Mg extraction and a cathodic peak at 0.8 V attributed to the Mg intercalation, with an average voltage of 1.9 V. Potential separation between the oxidation and reduction peak suggests the existence of an overpotential, mainly due to a surface film formation at the $Mg(TFSI)_2$ diglyme electrolyte/Mg interface, which is discussed in detail in our recent work.[17]

XAS Characterization. To understand the evolution of the vanadium's electronic structure at various charged/discharged states, vanadium K-edge and L-edge XANES were employed to characterize its oxidation state and local order of the electrodes and the electronic structure. Figure 2a and 2b (expanded view

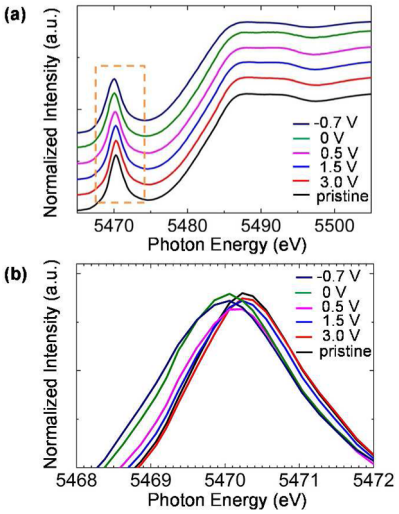

Figure 2. XANES spectra of $V_2O_5{\cdot}nH_2O$ at pristine, charged and discharged states. (a) Vanadium K-edge spectra for pristine (red), charged and discharged states of $V_2O_5{\cdot}nH_2O$ at 3 V, 1.5 V, 0.5 V, 0 V, and −0.7 V upon 10 cycles. (b) Expanded vanadium K-edge spectra of the pre-edge regime (enlarged from the highlighted area in panel a).

of Figure 2a) presented the normalized XANES spectrum of vanadium K-edge for the $V_2O_5{\cdot}nH_2O$ electrode at 3 V, 1.5 V, 0.5 V, 0 V, and −0.7 V (overdischarged) states, as well as its pristine state. Herein, a charged state corresponds to the 3 V sample, and a discharged state corresponds to the 0.5 and 0 V sample. An overdischarged state refers to the −0.7 V sample. 1.5 V is the open circuit voltage. The K-edge spectra revealed noticeable differences in the pre- and postedge region for the electrodes at discharged states versus charged states. The intensity of the pre-edge peak, considered to be a fingerprint for both valence and coordination of vanadium, is proportional to the deviation of the octahedral symmetry of the vanadium site,

DOI: 10.1021/acs.chemmater.6b00026
Chem. Mater. 2016, 28, 2962−2969

decreased in energy at discharged states (−0.7 V, 0 V, 0.5 V) as compared with the charged (3 V) and the pristine sample. According to the literature, the pre-edge features correspond to the dipole forbidden 1s to 3d transitions, which become increasingly permitted in nonoctahedral symmetry as the vanadium 3d states mix with the oxygen 2p states.[37] A decrease of the pre-edge intensity suggests an increase in the vanadyl (V═O) distance, and as a consequence the degree of distortion for the first oxygen atoms are elevated with a decrease of local symmetry.[28,29] The edge position, E_{edge}, determined by taking the first derivative of the normalized spectrum, has a relative energy shift of −0.35 eV, −0.26 eV, −0.21 eV, −0.04 eV, and 0.01 eV for electrodes at −0.7 V, 0 V, 0.5 V, 1.5 V, and 3.0 V, respectively, suggesting various degrees of vanadium reduction. The position of the three peaks past the edges represents characteristics of the V^{5+} feature.[38] Such peaks appear to be less well-defined for electrodes at discharged states, another sign of a mixed oxidation state of vanadium.[31]

Complementary XANES of vanadium L-edge and oxygen K-edge were performed to further explore the structural changes, shown in Figure 3a and 3b. The spectrum for the pristine $V_2O_5{\cdot}nH_2O$ sample is in good agreement with the previously reported V_2O_5 structure, and the two peaks centered at 518 and 525 eV are the V L_3 and L_2 peaks corresponding to transitions from V $2p_{3/2}$ and V $2p_{1/3}$ directly to the open V 3d states.[38] The V L_3 peak showed considerable fine structure in agreement with the reported literature.[40−42] Peak separation between V L_3 and L_2 was less prominent for discharged samples suggesting a decrease in valence upon Mg insertion. Both electron yield (Figure 3a) and fluorescence yield spectra (Figure 3b) displayed a clear shift to lower energy for discharged $V_2O_5{\cdot}nH_2O$ corresponding to a reduction of the vanadium valence from 5+. For instance, fully discharged $V_2O_5{\cdot}nH_2O$ showed an ∼0.4−0.5 eV shift to lower scale in reference to the pristine state. According to the literature,[41] an ∼1 eV shift corresponds to V^{5+} converted to V^{4+}, as demonstrated by the spectra of the VO_2 reference[39,40] with the pristine $V_2O_5{\cdot}nH_2O$ (Figure 3a). As a result, vanadium valence evolution from +5 to +4.5 upon discharge corresponded to a 0.25 Mg insertion per mole of $V_2O_5{\cdot}nH_2O$, and this finding is consistent with the electrochemical cycling results. Similar shifts of vanadium L-edge are observed for the fluorescence yield spectra indicating that the surfaces are undergoing the similar transition as the bulk. Vanadium L-edge and O K-edge suggest a reduction of vanadium and a change in hybridization of the oxygen state for the Mg intercalated $V_2O_5{\cdot}nH_2O$ cathode.

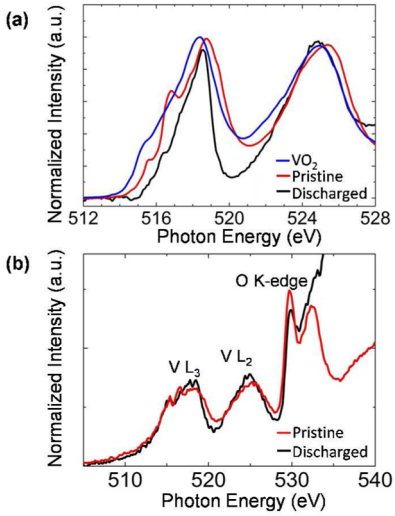

Figure 3. XANES spectra of $V_2O_5{\cdot}nH_2O$ at pristine, charged and discharged states. (a) Surface sensitive electron yield absorption spectra for pristine (red) and discharged (black) $V_2O_5{\cdot}nH_2O$ after 10 cycles. A VO_2 reference is included for comparison.[39] (b) Bulk sensitive fluorescence yield absorption spectra for pristine (red) and discharged (black) $V_2O_5{\cdot}nH_2O$.

Pair Distribution Function and Diffraction Analysis. Atomic pair distribution functions (PDF) analysis, a technique that is sensitive to local atomic ordering, is well-suited to study materials of limited structural coherence and is applied to investigate the structure evolution of the $V_2O_5{\cdot}nH_2O$ upon Mg intercalation. The PDF data for the electrodes showed well-defined peaks to intermediate length scales (ca. 44 Å) suggesting a high degree of local structural order, but reduced long-range order, as illustrated in Figure 4a. This longer range

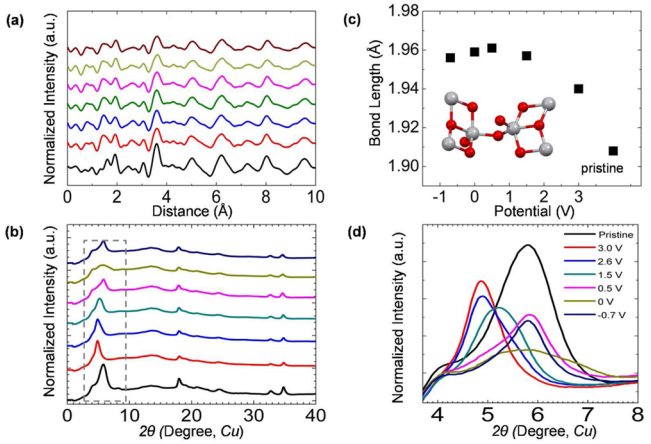

Figure 4. PDF data for $V_2O_5{\cdot}nH_2O$ cathodes derived from X-ray total scattering data. (a) Experimental PDFs of pristine, charged/discharged $V_2O_5{\cdot}nH_2O$ xerogel. (b) X-ray diffraction patterns of pristine and cycled $V_2O_5{\cdot}nH_2O$ at various charged/discharged states. Data was collected for electrodes upon 10 cycles. (c) The V−O peak position from the PDF data for pristine $V_2O_5{\cdot}nH_2O$ and (10×) cycled $V_2O_5{\cdot}nH_2O$ held at 3.0 V, 1.5 V, 0.5 V, 0 V, and −0.7 V. Inset is the local V_2O_5 structure, where red and gray balls represent oxygen and vanadium atoms, respectively. (d) An expanded view of the low angle diffraction data, which shows shifts in the first diffraction peak.

disorder is reflected in the corresponding X-ray diffraction data wherein only a few broad Bragg peaks were evident, as shown in Figure 4b. Evaluation of different vanadium oxide structural models against the PDF data indicates that the electrode structure is consistent with a monoclinic V_2O_5 phase (pristine electrode: $C2/m$, a = 11.860 Å, b = 3.624 Å, c = 11.042 Å, β = 85.5°). PDF fits to the experimental data were significantly improved by enlarging the atomic displacement parameters perpendicular to the V_2O_5 layer plane to account for turbostratic disorder between neighboring layers. The observed diffraction peaks correspond to the *00l* reflections, with the irregular peak intensities showing consistency with the turbostratic disorder. Such a bilayered V_2O_5 phase has been reported for a V_2O_5 xerogel,[25] δ-$Ag_{0.68}V_2O_5$,[18] and poly-(ethylene oxide)-V_2O_5,[43] with the possibility of different species occupying the interlayer space. While it was not possible to identify the interlayer species based on modeling of the PDF data alone, TGA analysis (SI) and the interlayer spacing suggest

DOI: 10.1021/acs.chemmater.6b00026
Chem. Mater. 2016, 28, 2962−2969

a composition of $V_2O_5{\cdot}1.8H_2O$ for the pristine material, with 0.6 water molecules per structure being coordinated to the V_2O_5 layers.[44−46]

The evolution in the bilayer spacing can be rationalized based on the different possible interstitial species and their interactions with the bilayer. Figure 5a listed interlayer spacing

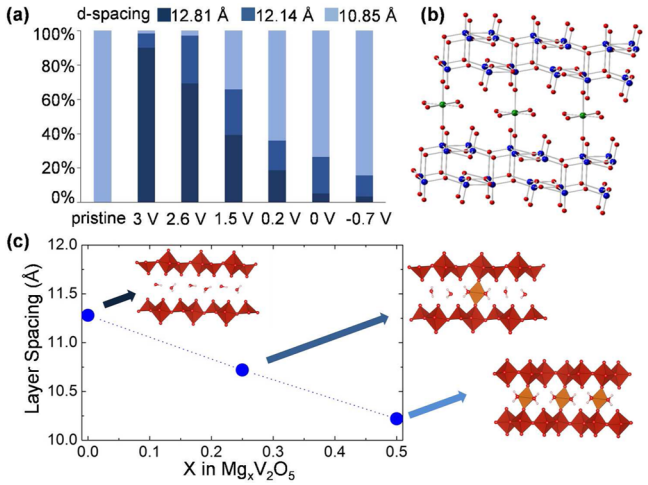

Figure 5. (a) The distribution of interlayer spacings for $V_2O_5{\cdot}nH_2O$ xerogels at different potentials. (b) A $Mg_{0.25}V_2O_5{\cdot}nH_2O$ structure with a layer spacing of ∼10.9 Å. Green, blue, and red balls stand for Mg, vanadium, and oxygen. (c) First-principles simulations of the bilayer spacing versus $V_2O_5{\cdot}nH_2O$ at different magnesiated states.

distributions versus the $V_2O_5{\cdot}nH_2O$ electrode at various charged/discharged states. (1) The shortest interlayer distance, 10.9 Å, at the fully discharged states is ascribed from the attraction between the V_2O_5 layers with the Mg complex. Similar interlayer spacings have been reported for the solid state synthesized $M_xV_2O_5{\cdot}nH_2O$ (where M is Mg, Ni, or Ca) structure with the metal cations bridging the V_2O_5 layers,[47] and in this case an octahedral M cation directly bridges the V_2O_5 layers.[48] Consequently, Mg intercalation can be associated with contraction of the V_2O_5 interlayer spacing as presented in Figure 5b. (2) The largest interlayer spacing, 12.8 Å, occurs for the fully charged electrode without Mg^{2+}. Not only does the expanded layer distance result from relaxation or reduced Mg-bridging of the V_2O_5 layers but also may reflect intercalation of nonbonding guest species. These are the largest interlayer spacing approaches that are found in V_2O_5 bilayer systems with organic molecules in the interlayer region,[43] including V_2O_5 with interstitial poly(ethylene oxide) which has an interlayer spacing of 13.2 Å.[43] For instance, diglyme or diglyme/TFSI-coordinated Mg can intercalate between layers — a conclusion that is supported by the ^{25}Mg NMR and ^{1}H NMR results. (3) The intermediate interlayer distance, 12.1 Å, largely occurs at intermediated states of charge/discharge (1.5 V) and can be possibly attributed to Mg orderings at intermediate Mg compositions. To further validate this point, first-principles calculations done on structures containing 1 mol of H_2O and a maximum of 0.5 mol of Mg per V_2O_5 display a stable Mg ordering at $Mg_{0.25}V_2O_5$ with a layer spacing value between that of the "fully magnesiated" ($Mg_{0.5}V_2O_5$) and fully demagnesiated structures as shown in Figure 5c. Though the trends displayed by the calculated structures cannot be benchmarked quantitatively, the qualitative trends agree with the experimentally measured values.

NMR Characterization. ^{25}Mg and ^{1}H MAS NMR spectroscopy were performed on electrochemically charged/discharged electrodes and the pristine state to provide insights into the Mg intercalation in the $V_2O_5{\cdot}nH_2O$ structure. Two distinct Mg resonances are identified in ^{25}Mg NMR spectra as illustrated in Figure 6a. The sharp and intense peak that

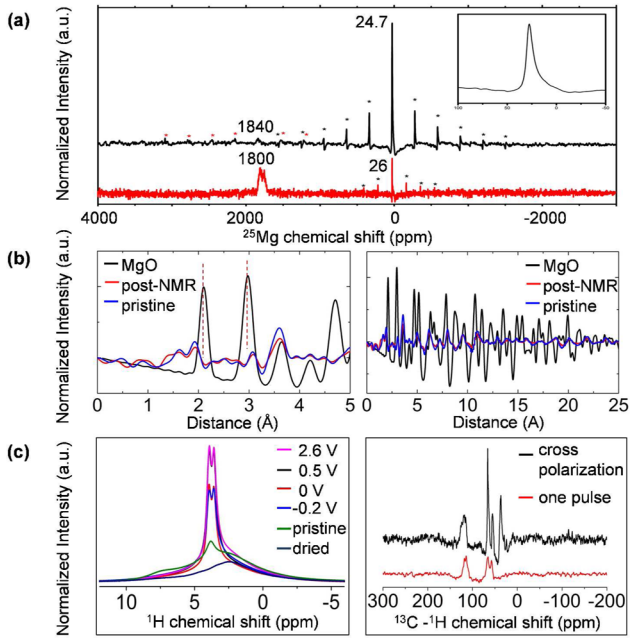

Figure 6. (a) ^{25}Mg MAS NMR collected for the electrochemically cycled $Mg_xV_2O_5$ sample (black, spinning at 16 kHz) and the solid state synthesized MgV_2O_5 sample (red, spinning at 10 kHz) at 19.89 T, with a spinning speed of 16 kHz using a 4 mm probe at 19 °C. Color coded spinning sidebands are marked with *. (b) PDF analysis for the post-NMR sample where the $V_2O_5{\cdot}nH_2O$ is discharged to 0 V. The right panel shows PDF data collected at a larger scale. (c) ^{1}H NMR for $V_2O_5{\cdot}nH_2O$ at various charged/discharged states (2.6 V, 0.5 V, 0 V, and −0.2 V). Electrodes were vacuum-dried at room temperature for 3 h before the measurements. NMR was performed at 7 T, 40 kHz. The ^{1}H NMR spectra are normalized to the weight of the active materials. Right panel: ^{13}NMR spectra of discharged sample (0 V). Data in red represents one pulse experiment, and data in black represents ^{1}H−^{13}C cross-polarization experiment. 115.2 ppm quartet is due to TFSI carbons.

appears at 24.7 ppm (fwhm = 3.5 ppm) with a large spinning sideband envelope (fwhm ∼ 500 ppm) is ascribed to the presence of an octahedrally coordinated Mg environment, which constitutes the Mg intercalation in a distorted/elongated/dynamic octahedral site with six Mg oxygen coordination. The asymmetry of the spectrum toward low frequency originates from a combined effect of the quadrapolar line shape and the distorted/elongated Mg−O coordination. The line shape of the central peak is in good agreement with the ^{25}Mg NMR spectra in similar disordered sites reported in the literature.[49] The same samples after NMR characterization are further characterized by PDF analysis as shown in Figure 6b, where the MgO structural model cannot be successfully refined, indicating no formation of MgO for the cycled electrode (dashed line). Furthermore, the significantly widened and more symmetric sideband envelope suggests a dynamic (and/or cocoordinated as will be discussed below) Mg site with a close proximity to a paramagnetic matrix as opposed to MgO impurity in the chemically synthesized sample (fwhm ∼150

DOI: 10.1021/acs.chemmater.6b00026
Chem. Mater. 2016, 28, 2962−2969

ppm with asymmetry). A minor Mg environment is observed at 1840 ppm, ∼5−10% compared to the diamagnetic site, where the large shift originates from Fermi-contact shift via spin density transfer from vanadium paramagnetic centers over oxygen p-orbitals to Mg s-orbitals. A similar shift is observed in the solid state synthesized MgV_2O_5 compound collected at the same magnetic field as shown in Figure 6a (red) for comparison.

In order to gain further insights into the intercalation structure, quantitative ^{1}H NMR spectra (normalized to the weight of the active material) were obtained for $V_2O_5{\cdot}nH_2O$ at various charged/discharged states as presented in Figure 6c (left panel), and ^{13}C NMR specta of the 0 V sample were acquired and shown (both one pulse experiment and cross-polarization experiment) in Figure 6c (right panel). The NMR spectrum of the pristine sample shows three main protonic features: the relatively sharp resonance at 2.83 ppm, which is assigned to the absorbed water molecules; resonance at 7.15 ppm, ascribed to the water molecules in the lattice; and the broad resonance at 2.45 ppm in the baseline assigned to lattice protons from −OH groups. To confirm these peak assignments, pristine $V_2O_5{\cdot}nH_2O$ was saturated in D_2O solution for 72 h to chemically exchange lattice H_2O with D_2O. An increase in the intensity of ^{1}H NMR resonance is observed at 4.8 ppm exclusively at the expense of 7.15 ppm resonance confirming the lattice water assignment. Electrochemically cycled $V_2O_5{\cdot}nH_2O$ showed two ^{1}H NMR resonances at 3.93 and 3.59 ppm, which are ascribed to the diglyme proton double peaks without lattice water and surface water proton signals. Due to the absence of diglyme signal from the diglyme soaked/dried sample in Figure 6c, it is clear that diglyme cointercalation is only shown to be possible when accompanied by Mg intercalation, suggesting a solvent molecules assisted Mg intercalation. To further confirm diglyme cointercalation, ^{13}C MAS cross-polarization and single pulse NMR spectra were acquired for the same discharged samples (0 V). The double diglyme carbon peaks at 66.5 and 56.0 ppm are clearly visible as shown in Figure 6c, confirming the existence of diglyme molecules in the $V_2O_5{\cdot}nH_2O$ lattice. In addition, significant proton bearing (increased intensity with ^{1}H−^{13}C cross-polarization experiment, Figure 6c black spectrum) aliphatic carbons appearing at 37.3 ppm are observed, indicative of electrochemical diglyme fragmentation due to decomposition. More interestingly, diglyme proton peak (Figure 6c) intensities change dramatically from 2.6 to 0 V to −0.2 V, indicative of removal of the diglyme molecules upon magnesiation, i.e. Mg-solvent cointercalation mechanism for this large *d*-spacing lattice. A plausible mechanism based on these experimental observations can be postulated as such: during the discharge step, a solvation shell coordinated Mg ion enters the $V_2O_5{\cdot}nH_2O$ bilayer and largely sheds the lattice water, resulting in magnesiation. Upon galvanostatic charge, Mg coordinated clusters are pulled out of the lattice, which is accompanied by free diglyme molecules and/or a reservoir of composed diglymes filling the lattice to compensate the void. This mechanism appears to be reversible at the expense of further electrolyte decomposition and Mg metal passivation via decomposed electrolyte species and the removal of lattice water.

CONCLUSIONS

To summarize, the Mg ion intercalation mechanism into the bilayered $V_2O_5{\cdot}nH_2O$ material has been determined through a combination of electrochemical techniques, X-ray absorption spectroscopy, pair distribution analysis, nuclear magnetic resonance spectroscopy, and the first principle calculations. The findings show direct evidence of reversible Mg insertion into $V_2O_5{\cdot}nH_2O$ and indicate that the process of Mg intercalation into $V_2O_5{\cdot}nH_2O$ involves the formation of new phases, which expands/contracts the bilayer spacing of the $V_2O_5{\cdot}nH_2O$. Interestingly, Mg insertion is shown to be accompanied by cointercalation of solvent molecules. Such solvent- assisted Mg intercalation can be explained by the preferable solvation of Mg in an oxygen rich donor environment.[50] Furthermore, electrochemically cycled $V_2O_5{\cdot}nH_2O$ suggested energetically favorable configurations for intercalated Mg, specifically an octahedral site with 6-fold oxygen coordinated around the Mg. Results summarized above highlight an in-depth description of Mg ion intercalation into the bilayered $V_2O_5{\cdot}nH_2O$ cathode with large interlayer spacing and provide a fundamental understanding for the design of fully reversible beyond Chevrel phase Mg-ion chemistries.

ASSOCIATED CONTENT

Supporting Information

The Supporting Information is available free of charge on the ACS Publications website at DOI: 10.1021/acs.chemmater.6b00026.

TGA analysis, additional ^{1}H, ^{13}C MAS NMR, and pair distribution analysis data (PDF)

AUTHOR INFORMATION

Corresponding Authors

*E-mail: burrell@anl.gov (A.K.B.).
*E-mail: saniyabnu@gmail.com (N.S.).

Author Contributions

A.K.B. guided this research. N.S. performed electrolyte synthesis, cell cycling, and electrochemical characterizations and prepared samples for PDF, XANES, and NMR characterizations. T.K., K.W.C., and P.J.C. performed the PDF measurements and data analysis. H.W. and B.K. worked on the NMR characterization. T.T.F. and J.W.F. helped with the XANES measurements. J.T.V. synthesized the cathode materials. D.L.P. helped with the laminate making. G.C. and G.S. advised and performed the simulation work.

Notes

The authors declare no competing financial interest.

ACKNOWLEDGMENTS

This work was supported as part of the Joint Center for Energy Storage Research (JCESR), an Energy Innovation Hub funded by the U.S. Department of Energy, Office of Science, Basic Energy Sciences. This research used resources at the Advanced Photon Source (beamline 20-BM-B, 4-ID-C, and 11-ID-B), the U.S. Department of Energy (DOE) Office of Science User Facilities operated for the DOE Office of Science by Argonne National Laboratory under Contract No. DE-AC02-06CH11357. The Materials Project (BES DOE Grant No. EDCBEE) is acknowledged for the simulation support. Premkumar Senguttuvan and Christopher Johnson were acknowledged for providing a chemically synthesized MgV_2O_5 sample. Andrew S. Lipton is acknowledged for high field NMR access at Environmental Molecular Sciences Laboratory at Pacific Northwest National Laboratory.

DOI: 10.1021/acs.chemmater.6b00026
Chem. Mater. 2016, 28, 2962−2969

REFERENCES

(1) Goodenough, J. B.; Park, K.-S. The Li-Ion Rechargeable Battery: A Perspective. *J. Am. Chem. Soc.* **2013**, *135*, 1167−1176.

(2) Saha, P.; Datta, M. K.; Velikokhatnyi, O. I.; Manivannan, A.; Alman, D.; Kumta, P. N. Rechargeable magnesium battery: Current status and key challenges for the future. *Prog. Mater. Sci.* **2014**, *66*, 1−86.

(3) Matsui, M. Study on electrochemically deposited Mg metal. *J. Power Sources* **2011**, *196*, 7048−7055.

(4) Ling, C.; Banerjee, D.; Matsui, M. Study of the electrochemical deposition of Mg in the atomic level: Why it prefers the non-dendritic morphology. *Electrochim. Acta* **2012**, *76*, 270−274.

(5) Liebenow, C. Reversibility of electrochemical magnesium deposition from Grignard solutions. *J. Appl. Electrochem.* **1997**, *27*, 221−225.

(6) Genders, J. D.; Pletcher, D. Studies using microelectrodes of the Mg(II)/Mg couple in tetrahydrofuran and propylene carbonate. *J. Electroanal. Chem. Interfacial Electrochem.* **1986**, *199*, 93−100.

(7) Brenner, A. Note on the Electrodeposition of Magnesium from an Organic Solution of a Magnesium-Boron Complex. *J. Electrochem. Soc.* **1971**, *118*, 99−100.

(8) Gregory, T. D.; Hoffman, R. J.; Winterton, R. C. Nonaqueous Electrochemistry of Magnesium: Applications to Energy Storage. *J. Electrochem. Soc.* **1990**, *137*, 775−780.

(9) Aurbach, D.; Lu, Z.; Schechter, A.; Gofer, Y.; Gizbar, H.; Turgeman, R.; Cohen, Y.; Moshkovich, M.; Levi, E. Prototype systems for rechargeable magnesium batteries. *Nature* **2000**, *407*, 724−727.

(10) Aurbach, D.; Gizbar, H.; Schechter, A.; Chusid, O.; Gottlieb, H. E.; Gofer, Y.; Goldberg, I. Electrolyte solutions for rechargeable magnesium batteries based on organomagnesium chloroaluminate complexes. *J. Electrochem. Soc.* **2002**, *149*, A115−A121.

(11) Aurbach, D.; Schechter, A.; Moshkovich, M.; Cohen, Y. On the mechanisms of reversible magnesium deposition processes. *J. Electrochem. Soc.* **2001**, *148*, A1004−A1014.

(12) Muldoon, J.; Bucur, C. B.; Oliver, A. G.; Zajicek, J.; Allred, G. D.; Boggess, W. C. Corrosion of magnesium electrolytes: chlorides - the culprit. *Energy Environ. Sci.* **2013**, *6*, 482−487.

(13) Gershinsky, G.; Yoo, H. D.; Gofer, Y.; Aurbach, D. Electrochemical and Spectroscopic Analysis of Mg2+ Intercalation into Thin Film Electrodes of Layered Oxides: V2O5 and MoO3. *Langmuir* **2013**, *29*, 10964−10972.

(14) Jiao, L. F.; Yuan, H. T.; Wang, Y. J.; Cao, H. S.; Wang, Y. M. Mg intercalation properties into open-ended vanadium oxide nanotubes. *Electrochem. Commun.* **2005**, *7*, 431−436.

(15) Yu, W.-h.; Da-zhi, W.; Bin, Z.; Shen-jun, W.; Li-xin, X. Insertion of bi-valence cations Mg 2+ and Zn 2+ into V 2O 5. *Solid State Commun.* **1987**, *61*, 271−273.

(16) Shterenberg, I.; Salama, M.; Gofer, Y.; Levi, E.; Aurbach, D. The challenge of developing rechargeable magnesium batteries. *MRS Bull.* **2014**, *39*, 453−460.

(17) Sa, N. W. H.; Proffit, L. D.; Lipson, L. A.; Key, B.; Liu, M.; Feng, Z.; Fister, T. T.; Ren, Y.; Sun, C.; Vaughey, T. J.; Fenter, A. P.; Persson, A. K.; Burrell, K. A. Is Alpha-V2O5 a Cathode Material for Mg Insertion Batteries? *J. Power Sources* **2016**, submitted.

(18) Wang, Y.; Cao, G. Developments in nanostructured cathode materials for high-performance lithium-ion batteries. *Adv. Mater.* **2008**, *20*, 2251−2269.

(19) Giorgetti, M.; Passerini, S.; Smyrl, W. H.; Berrettoni, M. Evidence of Bilayer Structure in V2O5 Xerogel. *Inorg. Chem.* **2000**, *39*, 1514−1517.

(20) Wei, Q.; Liu, J.; Feng, W.; Sheng, J.; Tian, X.; He, L.; An, Q.; Mai, L. Hydrated vanadium pentoxide with superior sodium storage capacity. *J. Mater. Chem. A* **2015**, *3*, 8070−8075.

(21) Lee, S. H.; DiLeo, R. A.; Marschilok, A. C.; Takeuchi, K. J.; Takeuchi, E. S. Sol Gel Based Synthesis and Electrochemistry of Magnesium Vanadium Oxide: A Promising Cathode Material for Secondary Magnesium Ion Batteries. *ECS Electrochem. Lett.* **2014**, *3*, A87−90.

(22) Stojkovic, I.; Cvjeticanin, N.; Markovic, S.; Mitric, M.; Mentus, S. Electrochemical Behaviour of V2O5 Xerogel and V2O5 Xerogel/C Composite in an Aqueous LiNO3 and Mg(NO3)(2) Solutions. *Acta Phys. Pol., A* **2010**, *117*, 837−840.

(23) Chernova, N. A.; Roppolo, M.; Dillon, A. C.; Whittingham, M. S. Layered vanadium and molybdenum oxides: batteries and electrochromics. *J. Mater. Chem.* **2009**, *19*, 2526−2552.

(24) Livage, J. Vanadium Pentoxide Gels. *Chem. Mater.* **1991**, *3*, 578−593.

(25) Petkov, V.; Trikalitis, P. N.; Bozin, E. S.; Billinge, S. J. L.; Vogt, T.; Kanatzidis, M. G. Structure of V2O5 center dot nH(2)O xerogel solved by the atomic pair distribution function technique. *J. Am. Chem. Soc.* **2002**, *124*, 10157−10162.

(26) Chupas, P. J.; Qiu, X.; Hanson, J. C.; Lee, P. L.; Grey, C. P.; Billinge, S. J. L. Rapid-acquisition pair distribution function (RA-PDF) analysis. *J. Appl. Crystallogr.* **2003**, *36*, 1342−1347.

(27) Chupas, P. J.; Chapman, K. W.; Lee, P. L. Applications of an amorphous silicon-based area detector for high-resolution, high-sensitivity and fast time-resolved pair distribution function measurements. *J. Appl. Crystallogr.* **2007**, *40*, 463−470.

(28) Avansi, W., Jr.; Ribeiro, C.; Leite, E. R.; Mastelaro, V. R. Vanadium Pentoxide Nanostructures: An Effective Control of Morphology and Crystal Structure in Hydrothermal Conditions. *Cryst. Growth Des.* **2009**, *9*, 3626−3631.

(29) Mansour, A. N.; Smith, P. H.; Baker, W. M.; Balasubramanian, M.; McBreen, J. A Comparative In Situ X-Ray Absorption Spectroscopy Study of Nanophase V 2 O 5 Aerogel and Ambigel Cathodes. *J. Electrochem. Soc.* **2003**, *150*, A403−A413.

(30) Farrow, C. L.; Juhas, P.; Liu, J. W.; Bryndin, D.; Bozin, E. S.; Bloch, J.; Proffen, T.; Billinge, S. J. L. PDFfit2 and PDFgui: computer programs for studying nanostructure in crystals. *J. Phys.: Condens. Matter* **2007**, *19*, 335219.

(31) Nabavi, M.; Taulelle, F.; Sanchez, C.; Verdaguer, M. Xanes and 51V Nmr study of vanadium-oxygen compounds. *J. Phys. Chem. Solids* **1990**, *51*, 1375−1382.

(32) Kresse, G.; Hafner, J. Ab initio molecular-dynamics for liquid-metals. *Phys. Rev. B: Condens. Matter Mater. Phys.* **1993**, *47*, 558−561.

(33) Kresse, G.; Furthmüller, J. Efficient iterative schemes for ab initio total-energy calculations using a plane-wave basis set. *Phys. Rev. B: Condens. Matter Mater. Phys.* **1996**, *54*, 11169−11186.

(34) Lee, K.; Murray, É. D.; Kong, L.; Lundqvist, B. I.; Langreth, D. C. Higher-accuracy van der Waals density functional. *Phys. Rev. B: Condens. Matter Mater. Phys.* **2010**, *82*, 081101.

(35) Klimeš, J.; Bowler, D. R.; Michaelides, A. Van der Waals density functionals applied to solids. *Phys. Rev. B: Condens. Matter Mater. Phys.* **2011**, *83*, 195131.

(36) Oka, Y.; Yao, T.; Yamamoto, N. Crystal Structures of Hydrated Vanadium Oxides withδ-Type V2O5Layers:δ-M0.25V2O5·H2O,M = Ca, Ni. *J. Solid State Chem.* **1997**, *132*, 323−329.

(37) Giorgetti, M.; Passerini, S.; Smyrl, W. H.; Mukerjee, S.; Yang, X. Q.; McBreen, J. In situ X-ray absorption spectroscopy characterization of V2O5 xerogel cathodes upon lithium intercalation. *J. Electrochem. Soc.* **1999**, *146*, 2387−2392.

(38) Velazquez, J. M.; Jaye, C.; Fischer, D. A.; Banerjee, S. Near Edge X-ray Absorption Fine Structure Spectroscopy Studies of Single-Crystalline V2O5 Nanowire Arrays. *J. Phys. Chem. C* **2009**, *113*, 7639−7645.

(39) Lee, S.; Meyer, T. L.; Park, S.; Egami, T.; Lee, H. N. Growth control of the oxidation state in vanadium oxide thin films. *Appl. Phys. Lett.* **2014**, *105*, 223515.

(40) Abbate, M.; de Groot, F. M. F.; Fuggle, J. C.; Ma, Y. J.; Chen, C. T.; Sette, F.; Fujimori, A.; Ueda, Y.; Kosuge, K. Soft-x-ray-absorption studies of the electronic-structure changes through the VO2 phase transition. *Phys. Rev. B: Condens. Matter Mater. Phys.* **1991**, *43*, 7263−7266.

(41) Zimmermann, R.; Claessen, R.; Reinert, F.; Steiner, P.; Hufner, S. Strong hybridization in vanadium oxides: evidence from photoemission and absorption spectroscopy. *J. Phys.: Condens. Matter* **1998**, *10*, 5697−5716.

DOI: 10.1021/acs.chemmater.6b00026
Chem. Mater. 2016, 28, 2962−2969

(42) Schmitt, T.; Duda, L.-C.; Augustsson, A.; Guo, J. -H.; Nordgren, J. Resonent Soft X-ray Emission Spectroscopy Of V2O3, VO2 and NaV2O5. *Surf. Rev. Lett.* **2002**, *09*, 1369.
(43) Liu, Y. J.; Degroot, D. C.; Schindler, J. L.; Kannewurf, C. R.; Kanatzidis, M. G. Interaction Of Poly(Ethylene oxide) in V2O5 Xerogel. *Chem. Mater.* **1991**, *3*, 992−994.
(44) Livage, J. Sol-gel chemistry and electrochemical properties of vanadium oxide gels. *Solid State Ionics* **1996**, *86*−*88*, 935−942.
(45) Aldebert, P.; Baffier, N.; Gharbi, N.; Livage, J. Layered structure of vanadium pentoxide gels. *Mater. Res. Bull.* **1981**, *16*, 669−676.
(46) Yao, T.; Oka, Y.; Yamamoto, N. Layered structures of vanadium pentoxide gels. *Mater. Res. Bull.* **1992**, *27*, 669−675.
(47) Oka, Y.; Yao, T.; Yamamoto, N. Crystal Structures and Lattice Distortions ofσ-Type Layered Vanadium Bronzes:σ-M0.25V2O5·H2O (M = Mg, Co, Ni). *J. Solid State Chem.* **1999**, *144*, 181−187.
(48) Shklover, V.; Haibach, T.; Ried, F.; Nesper, R.; Novák, P. Crystal Structure of the Product of Mg2+Insertion into V2O5Single Crystals. *J. Solid State Chem.* **1996**, *123*, 317−323.
(49) Cahill, L. S.; Hanna, J. V.; Wong, A.; Freitas, J. C. C.; Yates, J. R.; Harris, R. K.; Smith, M. E. Natural Abundance 25Mg Solid-State NMR of Mg Oxyanion Systems: A Combined Experimental and Computational Study. *Chem. - Eur. J.* **2009**, *15*, 9785−9798.
(50) Rajput, N. N.; Qu, X.; Sa, N.; Burrell, A. K.; Persson, K. A. The Coupling between Stability and Ion Pair Formation in Magnesium Electrolytes from First-Principles Quantum Mechanics and Classical Molecular Dynamics. *J. Am. Chem. Soc.* **2015**, *137*, 3411−3420.

DOI: 10.1021/acs.chemmater.6b00026
Chem. Mater. 2016, 28, 2962−2969